

# Electrostatically Induced Black Phosphorus Infrared Photodiodes

Wei Yan, Shifan Wang, Kaijian Xing, Sivacarendran Balendhran, Mike Tebyetekerwa, Kenji Watanabe, Takashi Taniguchi, Michael S. Fuhrer, Kenneth B. Crozier, and James Bullock\*

Homojunctions are key elements in many mainstream electronic devices. However, conventional dopant-based “pn” homojunctions are not easily achievable in new material families, such as the 2D materials. Several recent 2D material studies have shown that lateral pn homojunctions can instead be electrostatically induced using back gates localized to either the source or drain contacts. Here, a hBN-encapsulated black phosphorus dual-gate device containing a lateral pn homojunction, whose orientation can be switched via application of back gate voltages, is demonstrated. Importantly, this study extends the state-of-the-art for this architecture by characterizing the photoreponse under infrared ( $\lambda = 2.2 \mu\text{m}$ ) illumination. It is shown that when biased to form a homojunction, the device exhibits the photovoltaic effect, resulting in a specific detectivity of  $8.5 \times 10^8 \text{ cm Hz}^{1/2} \text{ W}^{-1}$  at 77 K under short-circuit conditions, and an open circuit photovoltage up to 175 mV at 77 K. Further, it is shown that the device can be operated in photoconductive mode, allowing a high responsivity of  $0.55 \text{ A W}^{-1}$ . This device is thus highly reconfigurable as it can be switched between photovoltaic and photoconductive modes of operation to prioritize low noise and fast response or high responsivity.

applications.<sup>[1–3]</sup> It exhibits a direct bandgap that can be tuned by controlling its number of layers ( $\approx 2 \text{ eV}$  for monolayer, to  $\approx 0.31 \text{ eV}$  for bulk),<sup>[2,4–6]</sup> by the application of strain (bulk bandgap of  $0.22 \text{ eV}$  for 1.21% tensile,  $0.53 \text{ eV}$  for 0.66% compressive),<sup>[7,8]</sup> by alloying with arsenic (bulk bandgap of  $0.269 \text{ eV}$  for 91% As),<sup>[9]</sup> and by embedding within an electric field (bulk bandgap of  $0.160 \text{ eV}$  under  $0.48 \text{ V nm}^{-1}$  field).<sup>[10]</sup> Its direct bandgap, low Auger coefficient, and low surface recombination velocity result in a high radiative efficiency,<sup>[11]</sup> which has already been exploited in IR light emitting diodes.<sup>[7,12–14]</sup> It exhibits a high carrier mobility, allowing the demonstration of detectors with GHz response speeds,<sup>[1,15]</sup> and anisotropic optical properties, which have been used to detect linear polarization.<sup>[4,16]</sup> Preliminary demonstrations of larger area bP devices have also been made using inkjet printing of solution dispersed bP inks,<sup>[17,18]</sup> although this remains an area of development.

## 1. Introduction

Black phosphorus (bP) has emerged as one of the most promising van der Waals materials for infrared (IR) optoelectronic

Unlike other van der Waals materials, where research has focused mainly on the monolayer to the few-layer regime,

W. Yan, S. Wang, S. Balendhran, K. B. Crozier, J. Bullock  
Department of Electrical and Electronic Engineering  
The University of Melbourne  
Parkville, Victoria 3010, Australia  
E-mail: [james.bullock@unimelb.edu.au](mailto:james.bullock@unimelb.edu.au)  
K. Xing, M. S. Fuhrer  
School of Physics and Astronomy  
Monash University  
Clayton, Victoria 3800, Australia  
M. Tebyetekerwa  
School of Chemical Engineering  
The University of Queensland  
Brisbane, Queensland 4072, Australia

K. Watanabe  
Research Center for Electronic and Optical Materials  
National Institute for Materials Science  
1-1 Namiki, Tsukuba 305-0044, Japan  
T. Taniguchi  
International Center for Materials Nanoarchitectonics  
National Institute for Materials Science  
1-1 Namiki, Tsukuba 305-0044, Japan  
M. S. Fuhrer  
Australian Research Council Centre of Excellence in Future Low-Energy  
Electronics Technologies (FLEET)  
Monash University  
Clayton, Victoria 3800, Australia  
K. B. Crozier  
School of Physics  
The University of Melbourne  
Parkville, Victoria 3010, Australia  
K. B. Crozier  
Australian Research Council (ARC) Centre of Excellence for  
Transformative Meta-Optical Systems (TMOS)  
The University of Melbourne  
Parkville, Victoria 3010, Australia

The ORCID identification number(s) for the author(s) of this article can be found under <https://doi.org/10.1002/adfm.202316000>

© 2024 The Authors. Advanced Functional Materials published by Wiley-VCH GmbH. This is an open access article under the terms of the [Creative Commons Attribution-NonCommercial](https://creativecommons.org/licenses/by-nc/4.0/) License, which permits use, distribution and reproduction in any medium, provided the original work is properly cited and is not used for commercial purposes.

DOI: 10.1002/adfm.202316000

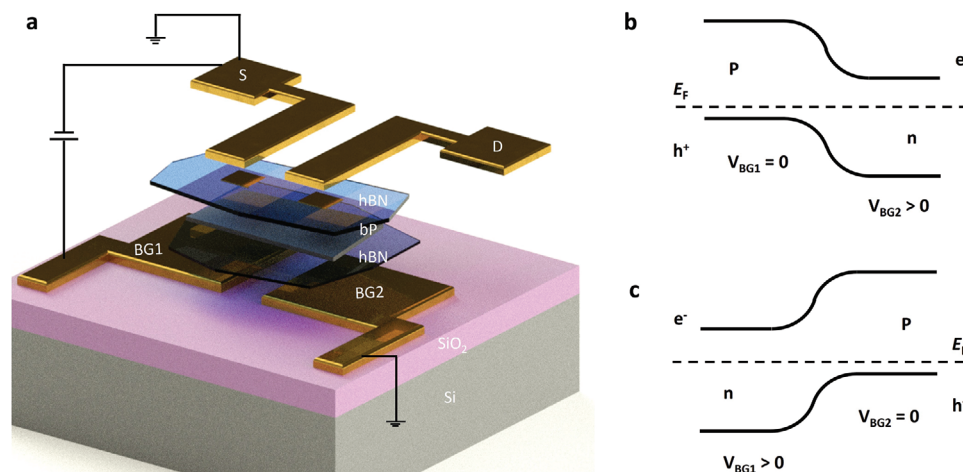


**Figure 1.** a) Exploded-view schematic diagram of hBN/bP/hBN dual-gate structure with two Cr/Au back gates on a Si/SiO<sub>2</sub> substrate. An example biasing configuration is shown by the black lines. b,c) Illustrative band diagrams of the device operating as a pn or np junction diode when a strong positive bias is applied to different back gates.

much of the research on bP has been in its bulk form (i.e.,  $> \approx 8$  layers).<sup>[6,19,20]</sup> This is especially true for demonstrations of photodetectors/light emitters in the mid-wave IR (MWIR) region.<sup>[4,9,14,21–23]</sup> These have been formed predominantly by stacking bulk bP with other 2D materials, creating functional heterojunctions, for example, with MoS<sub>2</sub>,<sup>[4,7,24]</sup> MoTe<sub>2</sub>,<sup>[25]</sup> WSe<sub>2</sub>,<sup>[26]</sup> and WS<sub>2</sub>.<sup>[27]</sup> An alternative approach to create junctions for light collection/emission is to instead electrostatically induce a homojunction within the bP absorber/emitter.<sup>[28]</sup> This can be achieved using localized rear gates under a bP channel, such as the dual-gate structure shown in **Figure 1**. In this structure, asymmetric potentials can be applied to the two gates, resulting in the formation of a lateral pn homojunction. **Figure 1a** shows a device schematic with an example biasing configuration. By applying a positive bias to back gate 1, while holding back gate 2 at zero bias, a lateral homojunction can be formed creating the band diagram shown in **Figure 1c**. The strong positive bias inverts the above channel region to n-type, from its typical p-type state. The direction of the junction can be reversed by switching the gate bias configuration as illustrated in **Figure 1b**. Several earlier studies have demonstrated this, or similar, device architectures on 2D materials. These include monolayer and few-layer transition metal dichalcogenide absorbers, such as MoS<sub>2</sub>, MoSe<sub>2</sub>, WS<sub>2</sub>, and WSe<sub>2</sub>,<sup>[29–33]</sup> as well as few-layer bP absorbers.<sup>[28]</sup> The efficacy of these electrostatically induced lateral pn homojunctions has been demonstrated in photodiodes, photovoltaic cells, and light-emitting diodes.<sup>[34–40]</sup> **Table 1** presents a comparison of recent studies utilizing dual-gate structures, together with their accompanying photodetector/photovoltaic figures-of-merit. At present, all these demonstrations have focused on visible wavelength applications.

In this study, we extend this family of devices into the IR region, demonstrating functionality to wavelengths as long as  $\lambda = 2.2 \mu\text{m}$ . Importantly, to be able to detect infrared wavelengths we utilize bulk bP at thicknesses of 10–20 nm, which is thin enough to be modulated by back gates, while still maintaining its bulk bandgap ( $E_g \approx 0.31 \text{ eV}$ ). This bP flake is encapsulated by two hexagonal boron nitride (hBN) layers that pro-

tect the bP flake from oxidation, with the bottom hBN layer also serving as a rear gate dielectric.<sup>[34]</sup> When biased as a photodiode, these devices achieve open circuit voltages higher than half bP's bulk bandgap, which is a promising demonstration given their early stage of development. In addition, it is shown that such devices can be easily switched between photodiode and photoconductor modes of operation, enabling reconfigurable detectors.

## 2. Results and Discussion

An optical micrograph of a representative hBN/bP/hBN dual-gate device on a Si/SiO<sub>2</sub> substrate is presented in **Figure 2a**. A detailed account of the fabrication procedure for these devices is provided in the Experimental Section and shown in **Figure S2** (Supporting Information). Briefly, the thin bP flake (10–20 nm) is encapsulated between two hBN layers (bottom layer 10–30 nm, top layer 10–60 nm), and transferred onto a set of two back gate Cr/Au electrodes, using a poly(methyl methacrylate) (PMMA) dry transfer process. Prior to transfer, two vias are etched into the top hBN layer and are filled with Au ( $\approx 25 \text{ nm}$ ) to form the source and drain contacts. Finally, Cr/Au lines and wire bonding pads are formed, by electron beam lithography and electron beam evaporation, at the abovementioned Au-filled vias. The hBN/bP/hBN sandwich structure serves primarily to reduce oxidation/degradation of the bP layer, which is known to be unstable in air.<sup>[2]</sup> To further explore the hBN/bP/hBN sandwich structure, cross-sectional scanning transmission electron microscopy (STEM), and energy-dispersive X-ray spectroscopy (EDX) was performed. Results from these measurements are provided in **Figure 2b,c**. The STEM image in **Figure 2b** shows three layers separated by thin amorphous interlayers. The layered nature of the bP and hBN can be clearly seen with interlayer spacings of 5.3 and 3.3 Å, respectively, which agree well with those reported in the literature.<sup>[41–43]</sup> The two thin ( $\approx 2 \text{ nm}$ ) interfacial layers, situated between the hBN and bP layers, are most likely PO<sub>x</sub> which is commonly found on the surface of bP due to unintentional oxidation of bP during fabrication. **Figure 2c** shows an image of

**Table 1.** 2D material devices featuring electrostatically induced lateral pn homojunctions.

Material	Bandgap [eV]	Excitation wavelength [nm]	Meas. condition	$V_{OC}$ [mV]	$I_{SC}$ [nA]	PCE [%]	$R$ [ $\text{mA W}^{-1}$ ]	Response time	Refs.
Monolayer $\text{WSe}_2$	$\approx 1.65$	532	295 K, Vacuum	650	1	0.005	210	-	[35]
Monolayer $\text{WSe}_2$	1.64	500–800	295 K, Vacuum	640	0.014	0.5	16	-	[34]
Monolayer $\text{WSe}_2$	1.65	640	295 K, Vacuum	700	0.41	0.01	0.24	$\approx 10$ ms	[36]
10-layer $\text{MoSe}_2$	1.41	AM1.5	Unspecified	700–850	0.606	14	$\approx 477$	-	[37]
4 nm $\text{WSe}_2$	$\approx 1.2$	530	295 K, Vacuum	400	30	-	-	-	[38]
9 nm $\text{MoTe}_2$	1	450	Unspecified temperature, Vacuum	300	0.4	0.57	$\approx 34$	-	[39]
3.6 nm $\text{MoTe}_2$	1	658	295 K, Ambient	420	8	2.98	1500	-	[40]
“Few-layer” bP	$< 1.31$	640	295 K, Vacuum	50	1	$< 0.001$	$\approx 0.26$	$\approx 2$ ms	[28]
12 nm bP	$\approx 0.31$	2200	77 K, Vacuum	175	32	0.04	7.92	$\approx 13$ $\mu\text{s}$	This work
12 nm bP	$\approx 0.31$	2200	295 K, Vacuum	74	5.1	0.01	1.26	$\approx 10$ $\mu\text{s}$	This work

the location (top) and elemental profile (bottom) of an EDX line scan across these interfaces. These confirm the identity of hBN and bP layers as well as the  $\text{PO}_x$  interlayers. The  $\text{PO}_x$  interlayers were likely formed during the exfoliation/transfer process, after that the hBN encapsulation prevented further oxidation until the TEM lamella was prepared  $\approx 1$  month later. Note that the measured bP thickness ( $\approx 12$  nm), and hBN bottom layer ( $\approx 15$  nm) that serves as the gate dielectric, are typical for devices reported in this study.

To investigate the effectiveness of the hBN/bP/hBN back gates, the dependence of the drain current on the gate voltage  $I_D-V_G$ , is measured. **Figure 3a,b** shows the  $I_D-V_G$  behavior when varying the voltage at back gate 1 and back gate 2, respectively (referred to henceforth as  $V_{BG1}$  and  $V_{BG2}$ ). Measurements are taken in the dark, under a drain source voltage  $V_{DS}$  of 10 mV (dashed

lines) and 100 mV (solid lines), at both 295 K (red curves) and at 77 K (blue curves). The device shows p-type behavior around  $V_G = 0$  V, as expected for bP.<sup>[9]</sup> Regardless of which back gate is used, a small n-type branch is seen at gate biases above  $V_G = 10$  V, confirming that it is possible to use either  $V_{BG1}$  or  $V_{BG2}$  to electrostatically create an n-type region in the bP layer. Significantly better characteristics are obtained at low temperatures. For example, an increase in the on/off drain current ratio from  $\approx 2$  to  $\approx 4$  orders of magnitude is measured when cooling from 295 to 77 K. This behavior is expected from a narrow bandgap material where thermal generation can significantly increase the carrier density with temperature.<sup>[44]</sup> We note that earlier devices revealed that applying back gate voltages of  $\approx 30$  V and above resulted in a high chance of breakdown for the bottom hBN layer.<sup>[45,46]</sup> As such, a back gate voltage limit of 26 V is used for this study.

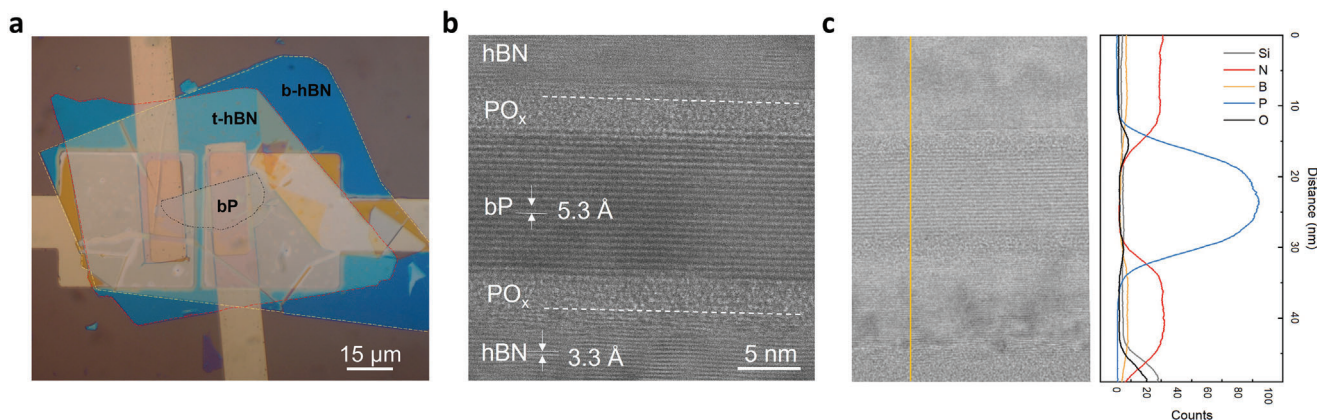


**Figure 2.** Images of the hBN/bP/hBN sandwich structure. a) Optical micrograph of a completed hBN/bP/hBN sandwich structure device. b) Cross-sectional STEM HAADF image of part hBN/bP/hBN sandwich structure showing the top-hBN, bP, and bottom-hBN layers. c) STEM HAADF (top) and EDX line scan of the Si, N, B, P, and O K edges.

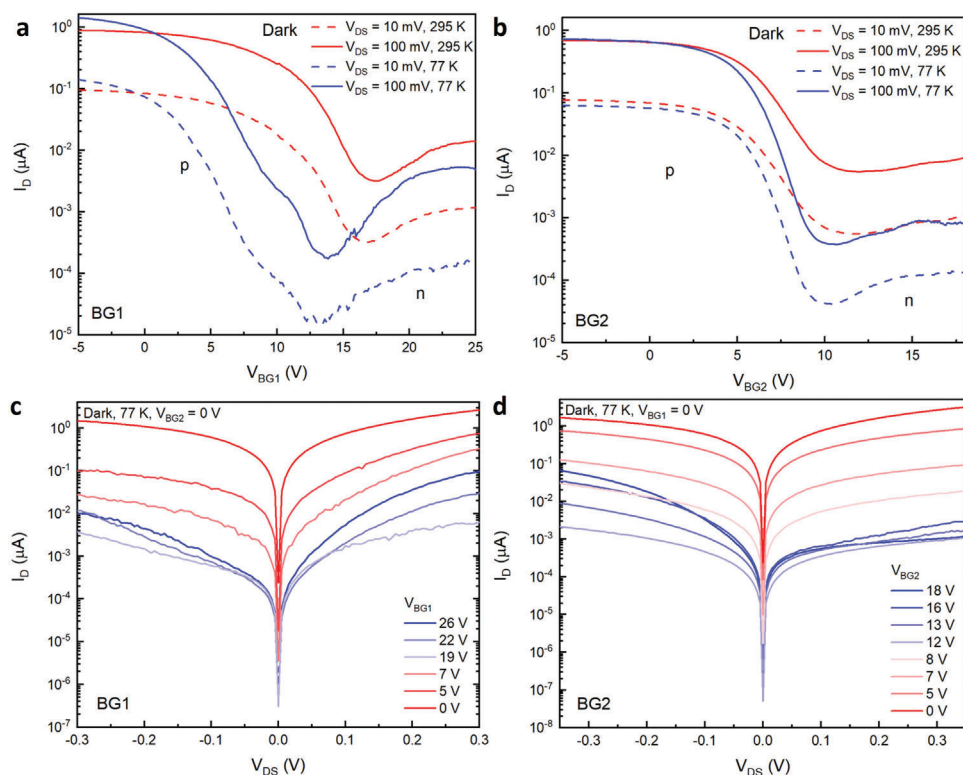


**Figure 3.** Dark current–voltage characteristic of bP dual-gate device. a,b)  $I_D$ – $V_G$  characteristics of bP dual-gate device modulating BG1 and BG2, respectively. These were measured in the dark at 295 K (red) and at 77 K (blue) under  $V_{DS} = 10$  mV and  $V_{DS} = 100$  mV bias. c)  $I_D$ – $V_D$  characteristics of bP dual-gate device operating in the dark at 77 K, for  $V_{BG1}$  ranging from 0 to 26 V. d)  $I_D$ – $V_D$  characteristics of bP dual-gate device operating in the dark at 77 K, for  $V_{BG2}$  varying from 0 to 18 V.

Based on the above results, a lateral pn homojunction exhibiting diode-like behavior should be achievable in either direction with sufficiently positive  $V_{BG1}$  or  $V_{BG2}$ . A family of  $I_D$ – $V_D$  curves measured at 77 K while varying  $V_{BG1}$  or  $V_{BG2}$  in isolation (i.e., whilst holding the other back gate at 0 V), is presented in Figure 3c,d, respectively. These two figures show  $I_D$ – $V_D$  behavior transitioning from Ohmic to rectifying behavior when  $V_{BG1}$  or  $V_{BG2}$  is increased beyond 7 or 12 V, respectively. The Ohmic characteristics seen around  $V_{BG1} = V_{BG2} = 0$  V, indicates the lack of any significant potential barriers at the bP/Au contacts. The rectification ratio seen with strong positive  $V_{BG1}$  or  $V_{BG2}$  is similar to that measured on bP/MoS<sub>2</sub> photodiodes,<sup>[4]</sup> and demonstrate that a lateral pn homojunction can be formed in either direction. Analogous, but less pronounced, rectification behavior can be seen when performing the same measurements at 295 K, as shown in Figure S3a (Supporting Information).

Next, we test the ability of these lateral pn homojunctions to collect photoexcited carriers generated with IR light. For these tests the device photoactive area is 36  $\mu\text{m}^2$ , and a  $\lambda = 2.2$   $\mu\text{m}$  laser is used to illuminate the device with a power density of  $\approx 11.2$   $\text{Wcm}^{-2}$ . Figure 4a shows the  $I_D$ – $V_D$  behavior under constant illumination, measured at 77 K. This plot's curves are measured under increasingly high  $V_{BG2}$  (while keeping  $V_{BG1} = 0$  V) showing the formation of an open circuit voltage ( $V_{OC}$ ) and short circuit current ( $I_{SC}$ ) under IR illumination, confirming its functionality as a photodiode at  $V_{BG2}$  above 10 V. It clearly shows the  $V_{OC}$  increase with  $V_{BG2}$  reaching a maximum of  $\approx 175$  mV. The

progression of the  $V_{OC}$  and  $I_{SC}$  with increasing  $V_{BG2}$  is provided in Figure 4b, showing a positive correlation with applied back gate bias. From these results, it is clear that a higher  $V_{BG2}$  increases the lateral pn homojunction built-in potential and provides higher junction collection probability. The saturation current  $I_0$  of this device can also be extracted above  $V_{BG2} = 13$  V. A comparison of  $I_0$  extracted using multiple techniques (see Supporting Information for explanation of extraction methods) is provided in Figure 4b, showing values  $\approx 0.3$  nA, which are comparable to those measured on similar devices previously.<sup>[28]</sup> The formation of a  $V_{OC}$  and  $I_{SC}$  can also be replicated when using  $V_{BG1}$  to form the lateral pn homojunction, as shown in Figure 4c. This plot compares typical  $I_D$ – $V_D$  sweeps in the dark/under IR illumination for high  $V_{BG1}$  or  $V_{BG2}$  biases, showing that similar  $V_{OC}$  and  $I_{SC}$  are formed in both directions. The power conversion efficiency (PCE) under a wavelength  $\lambda = 2.2$   $\mu\text{m}$  can be approximated to be  $\approx 0.04\%$  based on these measurements. This is a slight improvement over the efficiency observed in previous studies on electrostatically induced bP homojunctions (see Figure S4, Supporting Information for power–voltage curve).<sup>[28]</sup> A similar suite of measurements taken at 295 K, yielded lower results with a maximum  $V_{OC}$  of 74 mV (see Figure S3b,c, Supporting Information). While this result is lower than that measured at 77 K, likely due to the increase in the intrinsic carrier concentration,<sup>[47]</sup> it is still the highest reported for this device architecture to date (under similar illumination power). We note that the formation of a  $V_{OC}$  and  $I_{SC}$  confirms the device is not

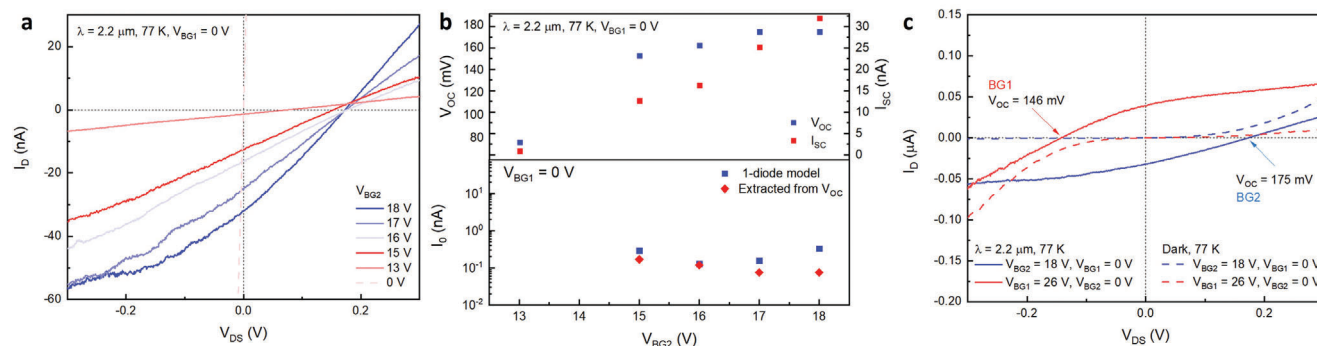


**Figure 4.** Current–voltage characteristic of bP dual-gate pn junction diode showing the photovoltaic effect under  $\lambda = 2.2 \mu\text{m}$  laser illumination. a) Back gate dependence of bP dual-gate pn junction showing photodiode like behavior with larger positive  $V_{BG2}$  biases. b) Top: The relationship between open-circuit voltage ( $V_{OC}$ ) and short-circuit current ( $I_{SC}$ ) against  $V_{BG2}$  at 77 K. Bottom: The relationship between extracted saturation current ( $I_0$ ) and  $V_{BG2}$ . c)  $I_D$ – $V_D$  characteristics under different  $V_{BG1}$  and  $V_{BG2}$  configurations (dark and  $\lambda = 2.2 \mu\text{m}$  laser illumination) at 77 K.

detecting light as a photoconductor under these bias conditions. However, it can be used as a photoconductor under  $V_{BG1} = V_{BG2} = 0 \text{ V}$  biasing conditions, showing a decrease in resistance under illumination, as highlighted in Figure S5 (Supporting Information). In the photoconductive mode the responsivity of the dual gate device is also found to be highly dependent on illumination intensity (see Figure S5b, Supporting Information), as is commonly found for 2D material photoconductors.<sup>[48–50]</sup>

To further standardize the performance of this device, photodetector signal-to-noise and speed figures-of-merit are also measured under  $\lambda = 2.2 \mu\text{m}$  illumination. The specific detectivity ( $D^*$ ) is calculated from measurements using the dark current and/or saturation current to estimate noise (details in the Experimental section).<sup>[51–53]</sup> Figure 5a shows the relationship between  $D^*$  and  $V_{BG2}$  (blue squares) or  $V_{BG1}$  (red circles) for a bP dual-gate device at 77 K (solid) and 295 K (hollow). As with the  $V_{OC}$  and  $I_{SC}$  trend discussed above, the detectivity increases with  $V_{BG2}$  or

$V_{BG1}$ . The highest  $D^*$  of  $8.5 \times 10^8 \text{ cm Hz}^{1/2} \text{ W}^{-1}$  is obtained when  $V_{BG1} = 26 \text{ V}$  and  $V_{BG2} = 0 \text{ V}$  at 77 K. As expected, the bP dual-gate device exhibits higher  $D^*$  at 77 K than at 295 K. A similar, but lower,  $D^*$  of  $\approx 2.7 \times 10^8 \text{ cm Hz}^{1/2} \text{ W}^{-1}$  is calculated for the device in the photoconductive mode (i.e., when  $V_{BG1} = V_{BG2} = 0 \text{ V}$ ) under  $V_{DS} = 350 \text{ mV}$ . As expected, the photoconductive mode produces a higher responsivity, reaching  $0.55 \text{ A W}^{-1}$  under  $V_{DS} = 500 \text{ mV}$ , which is offset by a higher noise current, but may still be useful in applications requiring high current. It is likely that this higher responsivity is partially attributable to the trap-induced photoconductive gain mechanism, which is commonly found in 2D material photoconductors.<sup>[54,55]</sup>

The  $D^*$  is also investigated as a function of  $V_{DS}$  when in the photovoltaic mode (i.e., when  $V_{BG1} = 0 \text{ V}$ ,  $V_{BG2} = 18 \text{ V}$ ). As expected, Figure 5b shows that low  $D^*$  values are obtained in the forward bias region, increasing to a peak  $D^*$  of  $\approx 7.2 \times 10^8 \text{ cm Hz}^{1/2} \text{ W}^{-1}$  at zero bias, with only slightly lower

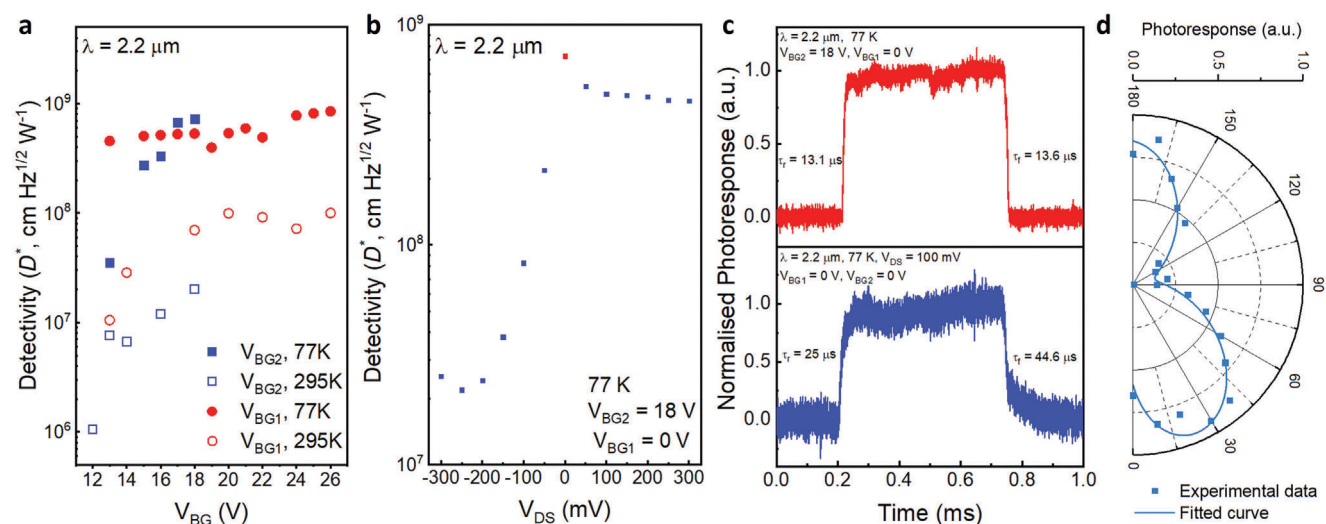


**Figure 5.** hBN/bP/hBN dual-gate device as a photodetector. a) The relationship between the specific detectivity  $D^*$  of a bP dual-gate device at  $V_{DS} = 0 \text{ V}$  and the magnitude of  $V_{BG1}$  (red) or  $V_{BG2}$  (blue) at 295 K (hollow) and 77 K (solid). b)  $D^*$  of a bP dual-gate device, with fixed back gate condition ( $V_{BG1} = 0 \text{ V}$ ,  $V_{BG2} = 18 \text{ V}$ ), under different  $V_{DS}$  bias conditions at 77 K. c) Frequency response of hBN/bP/hBN dual-gate device under photovoltaic (top) and photoconductive (bottom) modes of operation. d) Normalized photoresponse under IR illumination as a function of linear polarization angle.

$D^*$  obtained in the reverse bias region. It should be noted that the above  $D^*$  values are upper limit estimates due to the use of calculated idealized noise rather than utilizing noise spectral density measurements. In reality, the noise is likely also affected by non-fundamental noise mechanisms, such as flicker noise, which can be significantly higher than the calculated idealized noise.<sup>[56]</sup> In addition, no attempt was made to optimize the optical structure of the device. Light absorption enhancement strategies could be combined with this structure to greatly enhance the bP layer absorption, such as integrating structures that support surface plasmons,<sup>[57]</sup> matching the absorption wavelength with exciton resonances,<sup>[58]</sup> or by simply tuning the layer thicknesses in the stack. The latter of these is explored in supporting information Figure S1 (Supporting Information) and shows that a greater than 10 $\times$  improvement could be obtained by altering the hBN layer thicknesses in isolation.

Next, the frequency response of the bP dual-gate device is investigated by subjecting it to electrically modulated (1 kHz)  $\lambda = 2.2 \mu\text{m}$  illumination at 77 K. The device's response under different back gate biasing modes is tested. As shown in Figure 5c, under the photovoltaic mode (i.e., when  $V_{\text{BG1}} = 0 \text{ V}$ ,  $V_{\text{BG2}} = 18 \text{ V}$ ), the rise and fall times of the device are less than 13  $\mu\text{s}$ , limited in this case by our instrumentation. We expect that the actual response times of the device in the photovoltaic mode, that is, had we not been limited by instrumentation, are much shorter.<sup>[23,24]</sup> Under the photoconductor mode (i.e., when  $V_{\text{BG1}} = V_{\text{BG2}} = 0 \text{ V}$ ,  $V_{\text{DS}} = 100 \text{ mV}$ ), the rise and fall time are found to be 25 and 44.6  $\mu\text{s}$ , respectively. The slower response speed of photoconductors is commonly explained by a greater dependency on the lifetime of traps in the bP channel.<sup>[53,55]</sup> For context to the above figures of merit, a compilation of results for 2D material detectors in the 1–3.5  $\mu\text{m}$  IR region has been included in Table S1 (Supporting Information). It can be seen that speed and responsivity/detectivity results obtained in the photoconductive and photodiode modes of operation fall within the range of reported values for 2D material-based photodetectors in the short-wave IR wavelength space. Finally, the polarization dependence of a representative bP dual-gate device was measured using an unpolarized broadband IR illumination source with a wire grid polarizer. Figure 5d shows the expected strong dependence of the photoresponse on the linear polarization angle that is characteristic of bP's anisotropic crystal structure.<sup>[4,16,59]</sup>

### 3. Conclusion

In this study, hBN/bP/hBN dual-gate devices are fabricated and demonstrated as IR photodetectors. It is shown that applying sufficiently large bias to one of the two rear gates, while holding the other at zero bias, leads to the formation of a lateral pn junction. Under IR ( $\lambda = 2.2 \mu\text{m}$ ) illumination, this lateral pn junction exhibits the photovoltaic effect yielding a  $V_{\text{OC}}$  as high as 175 and 74 mV, at 77 and 295 K, respectively. These are the highest values reported for bP based dual-gate devices to date. When being used to detect light, under zero source-drain voltage, a specific detectivity of  $8.5 \times 10^8$  and  $2 \times 10^7 \text{ cm Hz}^{1/2} \text{ W}^{-1}$  is measured at 77 and 295 K, respectively. By modulating the back gate voltage, the dual-gate structure also allows switching between photoconductive and photovoltaic modes of operation. This allows a tradeoff between low noise/fast response (photovoltaic mode) and high

responsivity (photoconductive mode). This development extends the application of dual-gate van der Waals materials photodetectors into the IR wavelength space.

### 4. Experimental Section

**Device Fabrication/Imaging:** hBN/bP/hBN dual-gate devices were fabricated on Si/SiO<sub>2</sub> substrates pre-patterned with Cr (5 nm) / Au (45 nm) back gates defined by electron beam lithography (EBL). The bottom hBN layer was first transferred onto the pre-patterned substrate, positioned over a set of back dual-gates, using a poly(methyl methacrylate) (PMMA) based dry transfer process. In a separate process, a stack comprising the top hBN layer and bP was prepared. Vias in the top hBN layer were patterned using standard UV photolithography and then etched with reactive ion etching (RIE) (Oxford Instrument PLASMALAB100 ICP380). This etching step involved subjecting patterned hBN flakes to SF<sub>6</sub> plasma (IF-100, ICP-600) for 5 s to completely remove the unprotected hBN. After that, 25 nm of Au was deposited into the etched region of hBN via electron-beam evaporation. Then, bP flakes were exfoliated in a low oxygen/moisture environment and the top hBN layer with Au vias was transferred on top. Subsequently, the hBN/bP heterostructure was transferred onto the bottom-hBN to fabricate the hBN/bP/hBN dual-gate structure. Finally, source and drain regions were defined by EBL, and Cr (10 nm)/Au (60 nm) contacts were deposited via electron beam evaporation. Following the lift-off of Cr/Au in the non-patterned areas, the completed devices were mounted and wire-bonded into a chip carrier for characterization. The bP bulk crystals, sourced from HQ graphene, have been recently measured to have carrier concentrations between  $6.5 \times 10^{11}$  and  $1.25 \times 10^{13} \text{ cm}^{-2}$  and Hall mobilities between 529 and 1615  $\text{cm}^2 \text{ V}^{-1} \text{ s}^{-1}$ .<sup>[60]</sup>

Transmission electron microscopy (TEM) and Scanning TEM (STEM) imaging were performed using Hitachi HF5000 Cs-corrected S/TEM system. The HF5000 is equipped with Gatan OneView camera for TEM imaging and Hitachi bright field (BF) and dark field (DF) detectors for STEM imaging. This microscope also had symmetrically opposed dual 100 mm<sup>2</sup> EDX detectors (Oxford) for high sensitivity elemental analysis. STEM images were captured using an illumination angle of  $\approx 32 \text{ mrad}$ . The STEM camera length was 37 cm. Collection angle ( $\beta$ ) was  $40 < \beta < 213$  (for DF imaging) and  $\beta < 3.3$  (for BF imaging). Sample for TEM imaging was prepared using NX5000 FIB.

**Device Characterization:** Dark current–voltage measurements of the hBN/bP/hBN dual-gate devices were measured using a Keysight B1500A semiconductor device parameter analyzer. Light current–voltage measurements were conducted using a  $\lambda = 2.2 \mu\text{m}$  laser (CNI MDL-H-2200) as the illumination source, and three source meters (Keithley 2425/2450). Rise/fall times were extracted by electrically modulating the laser illumination and capturing the time domain photocurrent, after amplification from a transimpedance amplifier (SR570), on an oscilloscope (Tektronix TDS 3034B). A schematic of this set-up can be found in the previous work, for example in Figure S9 (Supporting Information) of Ref. [61] The low/room temperature measurements mentioned above were performed in a cryostat with an IR transmissive zinc selenide window with/without liquid nitrogen cooling. External quantum efficiency was extracted from the light/dark current–voltage behavior using:<sup>[62]</sup>

$$\eta_e = \frac{Rhc}{q\lambda} \quad (1)$$

where  $R$  is the responsivity of the device, given by the photocurrent divided by the incident power ( $I_{\text{ph}}/P$ ),  $\lambda$  is the light wavelength,  $q$  is the elementary charge,  $h$  is the Planck constant, and  $c$  is the speed of light. Specific detectivity values were then calculated, based on the following equation:<sup>[53]</sup>

$$D^* = \frac{\eta_e \lambda q}{hc} \left( \frac{2q(I_D + 2I_0)}{A} \right)^{-1/2} \quad (2)$$

where  $A$  is the area of the device,  $I_D$  is the dark current, and  $I_0$  is the saturation current.

The polarization dependent photoresponse was measured using an unpolarized broadband IR illumination source (Thorlabs SLS 203L) together with a wire grid polarizer (WP25M-UB), to create a beam with a single linear polarization. This beam was mechanically chopped and directed onto a bP dual gate device and the linear polarization was varied by rotating the wire grid polarizer. The photocurrent from the bP dual gate device was amplified using a transimpedance pre-amplifier (SR570), then measured by a lock-in amplifier (SR510).

## Supporting Information

Supporting Information is available from the Wiley Online Library or from the author.

## Acknowledgements

This work was supported by the Australian Research Council (DE210101129 and DP210103428). K.X. and M.S.F. acknowledges support from the Australian Research Council (DP200101345). M.T. acknowledges support from the Centre for Microscopy and Microanalysis, UQ, for providing infrastructure for materials characterization and Joseph Fernando and Joseph Otte for assistance with S/TEM imaging and EDX analysis. K.B.C. acknowledges the support from the Australian Research Council (ARC) the Centre of Excellence for Transformative Meta-Optical Systems (CE200100010). J.B. acknowledges support from the Melbourne Centre for Nanofabrication (MCN) through their Technology Fellowship program. This work was performed in part at the Melbourne Centre for Nanofabrication (MCN) in the Victorian Node of the Australian National Fabrication Facility (ANFF).

## Conflict of Interest

The authors declare no conflict of interest.

## Data Availability Statement

The data that support the findings of this study are available from the corresponding author upon reasonable request.

## Keywords

2D material, black phosphorus, electrostatic doping, infrared photodiode, pn junction

Received: December 14, 2023

Revised: March 7, 2024

Published online:

- [1] L. Li, Y. Yu, G. J. Ye, Q. Ge, X. Ou, H. Wu, D. Feng, X. H. Chen, Y. Zhang, *Nat. Nanotechnol.* **2014**, *9*, 372.
- [2] F. Xia, H. Wang, Y. Jia, *Nat. Commun.* **2014**, *5*, 4458.
- [3] N. Youngblood, C. Chen, S. J. Koester, M. Li, *Nat. Photonics* **2015**, *9*, 247.
- [4] J. Bullock, M. Amani, J. Cho, Y.-Z. Chen, G. H. Ahn, V. Adinolfi, V. R. Shrestha, Y. Gao, K. B. Crozier, Y.-L. Chueh, A. Javey, *Nat. Photonics* **2018**, *12*, 601.
- [5] M. Huang, M. Wang, C. Chen, Z. Ma, X. Li, J. Han, Y. Wu, *Adv. Mater.* **2016**, *28*, 3481.

- [6] J. Qiao, X. Kong, Z.-X. Hu, F. Yang, W. Ji, *Nat. Commun.* **2014**, *5*, 4475.
- [7] H. Kim, S. Z. Uddin, D.-H. Lien, M. Yeh, N. S. Azar, S. Balendhran, T. Kim, N. Gupta, Y. Rho, C. P. Grigoropoulos, K. B. Crozier, A. Javey, *Nature* **2021**, *596*, 232.
- [8] G. Zhang, S. Huang, A. Chaves, C. Song, V. O. Özçelik, T. Low, H. Yan, *Nat. Commun.* **2017**, *8*, 14071.
- [9] M. Amani, E. Regan, J. Bullock, G. H. Ahn, A. Javey, *ACS Nano* **2017**, *11*, 11724.
- [10] C. Chen, X. Lu, B. Deng, X. Chen, Q. Guo, C. Li, C. Ma, S. Yuan, E. Sung, K. Watanabe, T. Taniguchi, L. Yang, F. Xia, *Sci. Adv.* **2020**, *6*, eaay6134.
- [11] N. Higashitarumizu, S. Z. Uddin, D. Weinberg, N. S. Azar, I. K. M. Reaz Rahman, V. Wang, K. B. Crozier, E. Rabani, A. Javey, *Nat. Nanotechnol.* **2023**, *18*, 507.
- [12] Y. Huang, J. Ning, H. Chen, Y. Xu, X. Wang, X. Ge, C. Jiang, X. Zhang, J. Zhang, Y. Peng, Z. Huang, Y. Ning, K. Zhang, Z. Zhang, *ACS Photonics* **2019**, *6*, 1581.
- [13] J. Zhang, M. Xie, Y. Zhang, J. Wang, X. Zhao, C. Chen, Q. Zhang, M. Xia, J. Li, Z. Dong, Y. Zhang, Z. Ren, T. Liu, A. Pan, S. Wang, K. Zhang, *Adv. Opt. Mater.* **2023**, *11*, 2300278.
- [14] Y. Zhang, S. Wang, S. Chen, Q. Zhang, X. Wang, X. Zhu, X. Zhang, X. Xu, T. Yang, M. He, X. Yang, Z. Li, X. Chen, M. Wu, Y. Lu, R. Ma, W. Lu, A. Pan, *Adv. Mater.* **2020**, *32*, 1808319.
- [15] H. Liu, A. T. Neal, Z. Zhu, Z. Luo, X. Xu, D. Tománek, P. D. Ye, *ACS Nano* **2014**, *8*, 4033.
- [16] X. Wang, A. M. Jones, K. L. Seyler, V. Tran, Y. Jia, H. Zhao, H. Wang, L. Yang, X. Xu, F. Xia, *Nat. Nanotechnol.* **2015**, *10*, 517.
- [17] G. Hu, T. Albrow-Owen, X. Jin, A. Ali, Y. Hu, R. C. T. Howe, K. Shehzad, Z. Yang, X. Zhu, R. I. Woodward, T.-C. Wu, H. Jussila, J.-B. Wu, P. Peng, P.-H. Tan, Z. Sun, E. J. R. Kelleher, M. Zhang, Y. Xu, T. Hasan, *Nat. Commun.* **2017**, *8*, 278.
- [18] H. Y. Jun, S. O. Ryu, S. H. Kim, J. Y. Kim, C. H. Chang, S. O. Ryu, C. H. Choi, *Adv. Electron. Mater.* **2021**, *7*, 2100577.
- [19] M. I. Ahamed, N. Shakeel, N. Anwar, in *Black Phosphorus: Synthesis, Properties and Applications* (Eds: Inamuddin, R. Boddula, A. M. Asiri), Springer, NY, USA **2020**, 139.
- [20] J. Yang, R. Xu, J. Pei, Y. W. Myint, F. Wang, Z. Wang, S. Zhang, Z. Yu, Y. Lu, *Light: Sci. Appl.* **2015**, *4*, e312.
- [21] X. Zong, H. Hu, G. Ouyang, J. Wang, R. Shi, L. Zhang, Q. Zeng, C. Zhu, S. Chen, C. Cheng, B. Wang, H. Zhang, Z. Liu, W. Huang, T. Wang, L. Wang, X. Chen, *Light: Sci. Appl.* **2020**, *9*, 114.
- [22] V. Tran, R. Soklaski, Y. Liang, L. Yang, *Phys. Rev. B* **2014**, *89*, 235319.
- [23] X. Chen, X. Lu, B. Deng, O. Sinai, Y. Shao, C. Li, S. Yuan, V. Tran, K. Watanabe, T. Taniguchi, D. Naveh, L. Yang, F. Xia, *Nat. Commun.* **2017**, *8*, 1672.
- [24] W. Yan, V. R. Shresha, Q. Jeangros, N. S. Azar, S. Balendhran, C. Ballif, K. Crozier, J. Bullock, *ACS Nano* **2020**, *14*, 13645.
- [25] T.-Y. Chang, P.-L. Chen, P.-S. Chen, W.-Q. Li, J.-X. Li, M.-Y. He, J.-T. Chao, C.-H. Ho, C.-H. Liu, *ACS Appl. Mater. Interfaces* **2022**, *14*, 32665.
- [26] P. Chen, T. T. Zhang, J. Zhang, J. Xiang, H. Yu, S. Wu, X. Lu, G. Wang, F. Wen, Z. Liu, R. Yang, D. Shi, G. Zhang, *Nanoscale* **2016**, *8*, 3254.
- [27] G. Dastgeer, M. F. Khan, G. Nazir, A. M. Afzal, S. Aftab, B. A. Naqvi, J. Cha, K.-A. Min, Y. Jamil, J. Jung, S. Hong, J. Eom, *ACS Appl. Mater. Interfaces* **2018**, *10*, 13150.
- [28] M. Buscema, D. J. Groenendijk, G. A. Steele, H. S. J. van der Zant, A. Castellanos-Gomez, *Nat. Commun.* **2014**, *5*, 4651.
- [29] H. Zeng, J. Dai, W. Yao, D. Xiao, X. Cui, *Nat. Nanotechnol.* **2012**, *7*, 490.
- [30] O. Lopez-Sanchez, D. Lembke, M. Kayci, A. Radenovic, A. Kis, *Nat. Nanotechnol.* **2013**, *8*, 497.
- [31] Y.-H. Chang, W. Zhang, Y. Zhu, Y. Han, J. Pu, J.-K. Chang, W.-T. Hsu, J.-K. Huang, C.-L. Hsu, M.-H. Chiu, T. Takenobu, H. Li, C.-I. Wu, W.-H. Chang, A. T. S. Wee, L.-J. Li, *ACS Nano* **2014**, *8*, 8582.
- [32] A. Pezeshki, S. H. H. Shokouh, T. Nazari, K. Oh, S. Im, *Adv. Mater.* **2016**, *28*, 3216.

- [33] Y. J. Zhang, J. T. Ye, Y. Yomogida, T. Takenobu, Y. Iwasa, *Nano Lett.* **2013**, *13*, 3023.
- [34] A. Pospischil, M. M. Furchi, T. Mueller, *Nat. Nanotechnol.* **2014**, *9*, 257.
- [35] B. W. H. Baugher, H. O. H. Churchill, Y. Yang, P. Jarillo-Herrero, *Nat. Nanotechnol.* **2014**, *9*, 262.
- [36] D. J. Groenendijk, M. Buscema, G. A. Steele, S. Michaelis De Vasconcellos, R. Bratschitsch, H. S. J. Van Der Zant, A. Castellanos-Gomez, *Nano Lett.* **2014**, *14*, 5846.
- [37] S. Memaran, N. R. Pradhan, Z. Lu, D. Rhodes, J. Ludwig, Q. Zhou, O. Ogunsolu, P. M. Ajayan, D. Smirnov, A. I. Fernández-Domínguez, F. J. García-Vidal, L. Balicas, *Nano Lett.* **2015**, *15*, 7532.
- [38] S. Aftab, I. Akhtar, Y. Seo, J. Eom, *ACS Appl. Mater. Interfaces* **2020**, *12*, 42007.
- [39] C. Zhu, X. Sun, H. Liu, B. Zheng, X. Wang, Y. Liu, M. Zubair, X. Wang, X. Zhu, D. Li, A. Pan, *ACS Nano* **2019**, *13*, 7216.
- [40] G. Wu, B. Tian, L. Liu, W. Lv, S. Wu, X. Wang, Y. Chen, J. Li, Z. Wang, S. Wu, H. Shen, T. Lin, P. Zhou, Q. Liu, C. Duan, S. Zhang, X. Meng, S. Wu, W. Hu, X. Wang, J. Chu, J. Wang, *Nat. Electron.* **2020**, *3*, 43.
- [41] S. M. Kim, A. Hsu, M. H. Park, S. H. Chae, S. J. Yun, J. S. Lee, D.-H. Cho, W. Fang, C. Lee, T. Palacios, M. Dresselhaus, K. K. Kim, Y. H. Lee, J. Kong, *Nat. Commun.* **2015**, *6*, 8662.
- [42] W. Gao, Y. Zhou, X. Wu, Q. Shen, J. Ye, Z. Zou, *Adv. Funct. Mater.* **2021**, *31*, 2005197.
- [43] X. Ling, H. Wang, S. Huang, F. Xia, M. S. Dresselhaus, *Proc. Natl. Acad. Sci. USA* **2015**, *112*, 4523.
- [44] M. Amani, C. Tan, G. Zhang, C. Zhao, J. Bullock, X. Song, H. Kim, V. R. Shrestha, Y. Gao, K. B. Crozier, M. Scott, A. Javey, *ACS Nano* **2018**, *12*, 7253.
- [45] Y. Hattori, T. Taniguchi, K. Watanabe, K. Nagashio, *ACS Nano* **2015**, *9*, 916.
- [46] Y. Hattori, T. Taniguchi, K. Watanabe, K. Nagashio, *ACS Appl. Mater. Interfaces* **2016**, *8*, 27877.
- [47] P. Löper, D. Pysch, A. Richter, M. Hermle, S. Janz, M. Zacharias, S. W. Glunz, *Energy Procedia* **2012**, *27*, 135.
- [48] G. Wu, X. Wang, Y. Chen, Z. Wang, H. Shen, T. Lin, W. Hu, J. Wang, S. Zhang, X. Meng, J. Chu, *Nanotechnology* **2018**, *29*, 485204.
- [49] L. Tao, Z. Chen, X. Li, K. Yan, J.-B. Xu, *npj 2D Mater. Appl.* **2017**, *1*, 19.
- [50] B. Kang, Y. Kim, W. J. Yoo, C. Lee, *Small* **2018**, *14*, 1802593.
- [51] C. Tan, M. Amani, C. Zhao, M. Hettick, X. Song, D. H. Lien, H. Li, M. Yeh, V. R. Shrestha, K. B. Crozier, M. C. Scott, A. Javey, *Adv. Mater.* **2020**, *32*, 2001329.
- [52] V. Krishnamurthi, H. Khan, T. Ahmed, A. Zavabeti, S. A. Tawfik, S. K. Jain, M. J. S. Spencer, S. Balendhran, K. B. Crozier, Z. Li, L. Fu, M. Mohiuddin, M. X. Low, B. Shabbir, A. Boes, A. Mitchell, C. F. McConville, Y. Li, K. Kalantar-Zadeh, N. Mahmood, S. Walia, *Adv. Mater.* **2020**, *32*, 2004247.
- [53] A. Rogalski, K. Adamiec, J. Rutkowski, in *Narrow-gap semiconductor photodiodes Photodetectors: Materials and Devices III*, SPIE Digital Library, Bellingham, WA, USA **1998**, p. 83.
- [54] L. Huang, B. Dong, X. Guo, Y. Chang, N. Chen, X. Huang, W. Liao, C. Zhu, H. Wang, C. Lee, K.-W. Ang, *ACS Nano* **2019**, *13*, 913.
- [55] H. Fang, W. Hu, *Adv. Sci.* **2017**, *4*, 1700323.
- [56] M. Long, A. Gao, P. Wang, H. Xia, C. Ott, C. Pan, Y. Fu, E. Liu, X. Chen, W. Lu, T. Nilges, J. Xu, X. Wang, W. Hu, F. Miao, *Sci. Adv.* **2017**, *3*, e1700589.
- [57] R. Kumar, A. Sharma, M. Kaur, S. Husale, *Adv. Opt. Mater.* **2017**, *5*, 1700009.
- [58] G. Zhang, S. Huang, A. Chaves, H. Yan, *ACS Nano* **2023**, *17*, 6073.
- [59] H. Yuan, X. Liu, F. Afshinmanesh, W. Li, G. Xu, J. Sun, B. Lian, A. G. Curto, G. Ye, Y. Hikita, Z. Shen, S.-C. Zhang, X. Chen, M. Brongersma, H. Y. Hwang, Y. Cui, *Nat. Nanotechnol.* **2015**, *10*, 707.
- [60] K. Welch, M. H. Doha, Z. P. Uttley, A. Fereidouni, A. Omolewu, J. Santos, M. El-Shenawee, H. O. H. Churchill, presented at 2022 IEEE USNC-URSI Radio Science Meeting (Joint with AP-S Symposium), Denver, CO, USA, **2022**, pp. 31-33.
- [61] S. Balendhran, M. Taha, S. Wang, W. Yan, N. Higashitarumizu, D. Wen, N. S. Azar, J. Bullock, P. Mulvaney, A. Javey, K. B. Crozier, *Adv. Funct. Mater.* **2023**, *33*, 2301790.
- [62] S. Wang, A. Ashokan, S. Balendhran, W. Yan, B. C. Johnson, A. Peruzzo, K. B. Crozier, P. Mulvaney, J. Bullock, *ACS Nano* **2023**, *17*, 11771.